Ultrasound-Guided Mechanical High-Intensity Focused Ultrasound (Histotripsy) Through an Acoustically Permeable Polyolefin-Based Cranioplasty Device

Lauren Ruger, Maya Langman, Renata Farrell, John H. Rossmeisl, Francesco Prada, and Eli Vlaisavljevich

***Abstract*—Histotripsy is a non-thermal focused ultrasound therapy in development for the non-invasive ablation of cancerous tumors. Intracranial histotripsy has been limited by significant pressure attenuation through the skull, requiring large, complex array transducers to overcome this effect. *Objective:* Recently, a biocompatible, polyolefin-based cranioplasty device was developed to allow ultrasound (US) transmission into the intracranial space with minimal distortion. In this study, we investigated the *in vitro* feasibility of applying US-guided histotripsy procedures across the prosthesis. *Methods:* Pressure waveforms and beam profiles were collected for single- and multi-element histotripsy transducers. Then, high-speed optical images of the bubble cloud with and without the prosthesis were collected in water and tissue-mimicking agarose gel phantoms. Finally, red blood cell (RBC) tissue phantom and excised brain tissue experiments were completed to test the ablative efficacy across the prosthesis. *Results:* Single element tests revealed increased pressure loss with increasing transducer frequency and increasing transducer-to-prosthesis angle. Array transducer measurements at 1 MHz showed average pressure losses of >50% across the prosthesis. Aberration correction recovered up to 18% of the pressure lost, and high-speed optical imaging in water, agarose gels, and RBC phantoms demonstrated that histotripsy bubble clouds could be generated across the prosthesis at pulse repetition frequencies of 50–500 Hz. Histologic analysis revealed a complete breakdown of brain tissue treated across the prosthesis. *Conclusion & Significance:* Overall, the results of this study demonstrate that the cranial prosthesis may be used as an acoustic window through which intracranial histotripsy can be applied under US guidance without the need for large transcranial array transducers.**

***Index Terms*—Brain, cranial window, cranioplasty, histotripsy, imaging, prosthesis, ultrasound.**

Manuscript received 2 February 2024; revised 23 April 2024; accepted 7 May 2024. Date of publication 10 May 2024; date of current version 26 August 2024. The work of Lauren Ruger was supported by the Virginia Tech Institute for Critical Technology and Applied Science Doctoral Scholars Program. This work was supported in part by the Focused Ultrasound Foundation under Grant FUS848 and in part by the American Kennel Club Canine Health Foundation under Grant 2907. *(Corresponding author: Lauren Ruger.)*

Lauren Ruger is with the Department of Biomedical Engineering and Mechanics, Virginia Polytechnic Institute and State University, Blacksburg, VA 24061 USA (e-mail: larnold24@vt.edu).

Maya Langman was with the Virginia Tech Carilion School of Medicine USA. She is now with the Department of Neurosurgery, Medical College of Wisconsin USA.

Renata Farrell is with the Department of Materials Science and Engineering, Virginia Polytechnic Institute and State University, USA.

John H. Rossmeisl is with the Department of Small Animal Clinical Sciences, Virginia-Maryland College of Veterinary Medicine, USA.

Francesco Prada is with the Department of Neurosurgery, Fondazione IRCCS Istituto Neurologico C. Besta, Italy.

Eli Vlaisavljevich is with the Department of Biomedical Engineering and Mechanics, Virginia Polytechnic Institute and State University, USA.

This article has supplementary downloadable material available at https://doi.org/10.1109/TBME.2024.3399688, provided by the authors.

Digital Object Identifier 10.1109/TBME.2024.3399688

I. Introduction

ULTRASOUND (US) is a versatile technology that is well-established as a safe and effective real-time bedside imaging modality. More recently, focused ultrasound (FUS) has emerged as an effective treatment modality for a multitude of applications and is under development as an intervention for various neurologic disorders, including immunomodulation, neuromodulation, blood-brain barrier opening, tumor ablation, and targeted drug delivery [1]. While there are many potential applications for diagnostic and therapeutic US in the intracranial space, the human skull reflects or absorbs a large amount of the ultrasonic energy [2], [3], [4]. This decreases the acoustic transmission between US transducers and the targeted intracranial structures, which in turn limits the effectiveness of US for brain imaging and FUS therapies for neurological pathologies when applied through intact cranial bone [3], [5], [6]. Previous research has been conducted to develop cranial prostheses of various bioinert and biocompatible materials which can be used to replace a section of cranial bone and increase US transmission into intracranial structures [5], [7], [8].

Recently, an implantable, biocompatible, polyolefin-based cranioplasty device was developed by Intelligenza Trasparente S.R.L. (In.Tra., Milan, Italy) for the purpose of transmitting US into the intracranial space with minimal distortion for imaging and therapeutic purposes (In.Tra., Milan, Italy, PCT/EP2014/068837, human biocompatibility ISO-10993). A preliminary *in vitro* characterization study measured ultrasonic

energy transmission across the prosthesis using four single-element, focused transducers (500 kHz, 1 MHz, 2.5 MHz, and 5 MHz) and one diagnostic ultrasound probe (5.3 MHz) [9]. Considerably higher ultrasonic energy transmission (frequency-dependent pressure reduction of ~10-40%) was observed across the prosthesis when compared to intact cranial bone for all transducers tested [9]. More recently, the cranioplasty device has been investigated pre-clinically for ultrasonic blood brain barrier (BBB) opening [10] and clinically for long-term ultrasound imaging surveillance in a patient with multi-recurrent oligodendroglioma [11]. The feasibility of applying high-intensity focused ultrasound (HIFU) therapies, such as histotripsy and thermal HIFU, across the prosthesis has not yet been investigated.

Histotripsy is a non-thermal, non-invasive, and non-ionizing focused ultrasound ablation technique using an extracorporeal transducer to generate highly controlled, high pressure ultrasound pulses which constructively interfere at the transducer focus to generate acoustic cavitation [12], [13], [14], [15], [16], [17]. The resulting cavitation 'bubble clouds' mechanically disintegrate target tissues during histotripsy treatment through cyclically applied stresses and strains, resulting in complete cellular lysis within a precisely defined lesional zone [14], [15], [16], [18]. To date, histotripsy has shown promise for various clinical applications, including the ablation of solid malignancies of the prostate [19], kidney [20], pancreas [21], and liver [22], [23], [24]. Additionally, recent work investigating histotripsy as a neurological intervention is promising, with preliminary results demonstrating the ability of histotripsy to target through the skull [25], [26], [27], [28], [29] as well as to ablate healthy brain tissue [28], [29], [30] and brain tumors [31]. These studies, however, have largely required advanced histotripsy devices capable of overcoming ultrasonic attenuation by the skull [26], [27], [32], [33] and/or have relied on magnetic resonance imaging (MRI) for guidance [25], [28]. The development of techniques that allow for ultrasound-guided histotripsy to be applied intracranially could increase the accessibility of histotripsy ablation for brain tumors, especially in low resource settings or in patients with recurrent malignancies.

In this study, we investigated the feasibility of applying histotripsy treatment through a sonolucent cranioplasty device developed by Intelligenza Trasparente S.R.L. (In.Tra., Milan, Italy). First, the attenuation (focal pressure loss) and aberration (distortions to the transducer beam profiles) effects on the histotripsy pulses across the prosthesis were measured through a series of single element and multi-element array transducer tests. Then, the ability of two prototype histotripsy array transducers to generate cavitation bubble clouds across the prosthesis with and without aberration correction was explored in water and tissue-mimicking agarose gel phantoms. Finally, the capability of the current histotripsy system to achieve effective ablation across the prosthesis with real-time ultrasound guidance was characterized using red blood cells phantoms and excised porcine brain tissue. Based on the prior studies investigating ultrasound attenuation across the prosthesis [9], [10], [11], we hypothesized that histotripsy bubble clouds could be generated across the prosthesis at sufficiently high pressures to cause effective ablation in brain tissue. The results of this study lay the groundwork for further advancements in real-time, ultrasound-guided histotripsy for intracranial applications, particularly in settings where MRI-guidance is not available [34].

II. Methods

A. Study Design

This study was divided into three components to determine the feasibility of applying histotripsy therapy through an implantable, biocompatible, polyolefin-based cranioplasty device. First, the effects of the prosthesis on single element histotripsy pulses were measured under a range of frequencies and angles. Then, these findings were expanded to larger, multi-element histotripsy array transducers to determine the pressure loss and focal distortion effects of the prosthesis under clinically-relevant test conditions. Finally, the capacity of the current histotripsy system to achieve effective ablation across the prosthesis was characterized by optically imaging the cavitation bubble cloud and resulting ablation in agarose gel, red blood cell phantoms, and excised porcine brain tissues. Additionally, coaxial ultrasound imaging was implemented for all histotripsy array transducer tests to demonstrate the ability to visualize the bubble cloud across the prosthesis for ultrasound-guided procedures.

B. Cranial Prosthesis Properties

All experiments were performed using a flat, sterilizable, 4 mm thick, 3 cm x 6 cm (single element tests) or 6 cm x 6 cm (histotripsy array experiments) polyolefin-based cranioplasty device produced by Intelligenza Trasparente S.R.L. (Milan, Italy). The density and porosity of the prosthesis are 0.93 g/cm^3 and 0.44 g/cm^3, respectively [9].

C. Histotripsy System

Custom single element histotripsy transducers with fundamental frequencies of 500 kHz, 1 MHz, and 3 MHz were used to determine the attenuation (focal pressure loss) and aberration (distortions to the transducer beam profiles) effects on histotripsy pulses across the prosthesis. Single element transducers were produced in-house and composed of 20 mm diameter piezoelectric discs, ABS-like lenses focused to 78 mm and produced by stereolithography (SLA) (Proto Labs, Inc., Maple Plain, MN, USA), and custom matching layers to reduce the acoustic impedance between the piezoelectric disc and the polymer lens.

Two multi-element histotripsy array transducers were also utilized to determine the effects of the prosthesis on aggregate pulse behaviors relevant to histotripsy therapy. First, an 8 element, 1 MHz transducer designed to deliver treatment through an open cranial window in a porcine intracerebral hemorrhage model was used [35]. Then, a larger, 16 element, 1 MHz transducer capable of generating higher focal pressures was tested to highlight potential aberration and attenuation differences across the prosthesis for different therapy transducers. Additionally, a phased array ultrasound imaging probe with a frequency range of 3–8 MHz (P8-3L10SI-6, Telemed, Vilnius, Lithuania) was coaxially aligned within the 16 element transducer to examine

TABLE I
HISTOTRIPSY ARRAY TRANSDUCER DETAILS

Histotripsy System	Depth to Focus (mm)	Aperture Size (mm)		F-number (mm)		FWHM (mm)	
1 MHz, 8 elements	45.5	72.5		0.63		*Transverse*	1.25
						Elevational	1.25
						Axial	5.2
1 MHz, 16 elements	58.0	*Transverse*	66.7	*Transverse*	0.87	*Transverse*	1.2
		Elevational	82.7	*Elevational*	0.70	*Elevational*	1.0
						Axial	4.25

The differences between the two multi-element histotripsy systems tested are highlighted using a breakdown of their critical characteristics (frequency, number of elements, aperture, f-number, and full-width half-maximum (FWHM)).

whether the bubble cloud could be visualized across the prosthesis using real-time ultrasound. Both transducers were populated using 1 MHz elements, as described above. A frequency of 1 MHz was chosen for all histotripsy array tests based on past work demonstrating the high precision of the 1 MHz bubble cloud [36] as well as the intermediate pressure loss previously measured across the prosthesis using a 1 MHz single element transducer [9]. Transducer details are summarized in Table I, and all transducers (single and multi-element) were driven using single cycle histotripsy pulses.

Prior to prosthesis tests, both array transducers were characterized as previously described [37], [38]. Briefly, free-field focal pressure waveforms were measured in degassed water using a high-sensitivity reference rod hydrophone (HNR-0500, Onda Corp., Sunnyvale, CA, USA) and a cross-calibrated custom-built fiber optic probe hydrophone (FOPH) aligned at the transducer's focus. The rod hydrophone was used to measure the lateral, elevational, and axial 1-D beam profiles of the 8 element and 16 element transducers at peak negative pressures (p-) of ~2.2 MPa and ~1.5 MPa, respectively. The measured full-width half-maximum (FWHM) dimensions for each transducer are given in Table I. Next, focal pressures were measured directly with the FOPH up to a peak negative pressure of ~20 MPa. At peak negative pressures greater than 20 MPa, the focal pressure was estimated by summing measurements from half and quarter subsets of the elements to prevent cavitation from forming on the fiber [39]. All waveforms were measured using a Tektronix TBS2000 series oscilloscope at a sample rate of 500 MS/s, averaged over 512 pulses, and recorded in MATLAB (The MathWorks, Natick, MA, USA).

All histotripsy transducers (single and multi-element) were driven using a custom high-voltage pulser designed to generate single cycle histotripsy pulses, powered by a high voltage DC power supply (GENH750W, TDK-Lambda, National City, CA, USA), and controlled by a preprogrammed field-programmable gate array (FPGA) board (Altera DE0-Nano Terasic Technology, Dover, DE, USA) and a custom MATLAB script (The MathWorks, Natick, MA, USA).

D. Single Element Experiments

1) Beam Profile and Pressure Waveform Characterization: Single element histotripsy transducers of frequencies

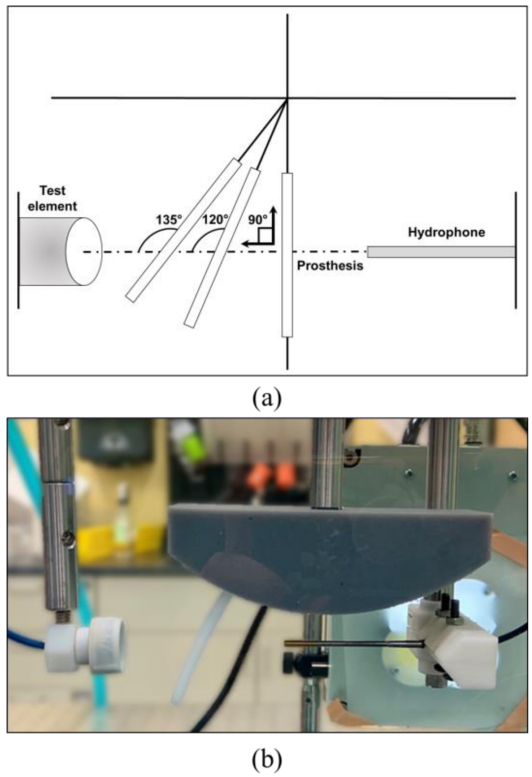

Fig. 1. Single element experimental set-up. (a) Schematic showing the single element test set-up. Three element frequencies were tested (500 kHz, 1 MHz, 3 MHz) with the prosthesis aligned at either 90°, 120°, or 135° relative to the test element. (b) Photograph of the test set-up showing the prosthesis aligned at 120° with a single histotripsy element.

500 kHz, 1 MHz, and 3 MHz were aligned perpendicularly to the prosthesis opposite a high-sensitivity rod hydrophone (HNR-0500, Onda Corp., Sunnyvale, CA, USA) in degassed water (<30% dissolved O_2) and tested to validate the results detailed in [9] with our experimental set-up. Then, the prosthesis was realigned at angles of 120° and 135° relative to the test element using a custom 3D printed holder and tested to mimic the various element angles in a histotripsy array transducer [Fig. 1].

Under each test condition (free-field versus prosthesis, various angles and frequencies), the rod hydrophone was affixed to a computer-guided 3D robotic positioner and used to measure the transverse and elevational 1D beam profiles of the single element

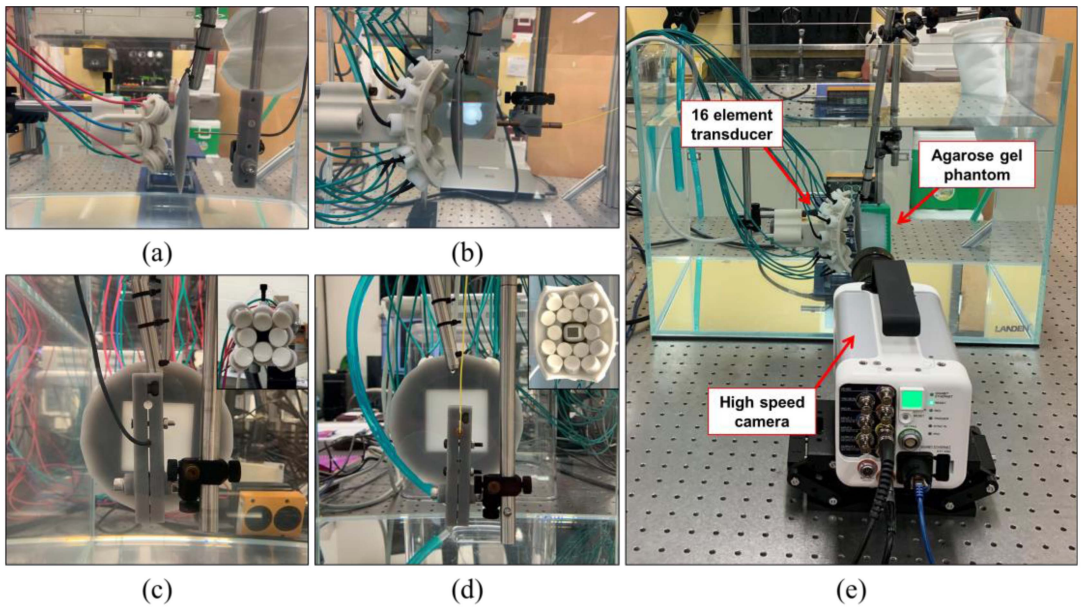

Fig. 2. Multi-element histotripsy array testing experimental set-up. (a), (c) 8 element, 1 MHz transducer (c, insert) aligned orthogonally to the prosthesis fixed in a 3D printed mock skull (grey) and the rod hydrophone. (b), (d) 16 element, 1 MHz transducer (d, insert) aligned orthogonally to the prosthesis fixed in the mock skull (grey) and the fiber optic probe hydrophone (FOPH). (e) Photograph of the test set-up for high speed imaging experiments using the 16 element transducer. The camera was aligned across from a constant light source and used to collect bubble cloud images for a range of pulse repetition frequencies (PRFs). An optically-translucent agarose gel phantom is aligned with the transducer focus.

transducer at the transducer's geometric focus by sweeping the hydrophone across each plane using 0.1 mm increments. Axial beam profiles were not collected for the single element transducers. At each location, pressure waveforms were measured using a Tektronix TBS2000 series oscilloscope at a sample rate of 500 MS/s, averaged over 128 pulses, and recorded in MATLAB. All beam profile tests were completed at the same transducer driving voltage.

Then, the rod hydrophone was realigned to the transducer focus and used to collect focal pressure waveforms under each test condition across a range of driving voltages (0 V to 90 V). At each voltage, the pressure waveform was measured using a Tektronix TBS2000 series oscilloscope at a sample rate of 500 MS/s, averaged over 128 pulses, and recorded in MATLAB. Next, peak negative pressures (p-) were calculated from each waveform, averaged within conditions, and compared between conditions. Individual data points were excluded from analysis if the p- was not clearly distinguishable from noise in the recorded waveform.

E. Histotripsy Array Transducer Experiments

1) Beam Profile and Pressure Waveform Characterization: Following single element characterization, multi-element histotripsy array transducers were also tested to determine the pressure loss and focal distortion effects of the prosthesis under therapy-relevant conditions. First, rod hydrophone measurements were completed in free-field and through prosthesis conditions as described above. Briefly, the rod hydrophone was secured to the computer-guided 3D robotic positioner and used to measure the lateral, elevational, and axial 1D beam profiles of each array transducer by incrementally repositioning the hydrophone in each direction using 0.1 mm spacing [Fig. 2(a), (c)]. At each location, pressure waveforms were measured using a Tektronix TBS2000 series oscilloscope at a sample rate of 500 MS/s, averaged over 128 pulses, and recorded in MATLAB. Beam profiles were measured at the same driving voltage for prosthesis and no prosthesis tests (15 V, 8 element transducer; 10 V, 16 element transducer).

After realigning the rod hydrophone to the transducer focus, focal pressure waveforms for each transducer without and with the prosthesis (aligned perpendicularly) were recorded across a range of driving voltages until the maximum measurable pressure with the rod hydrophone was reached ($\sim$2.5 MPa p-). Tested driving voltages ranged from 0 V to 16.5 V without the prosthesis and 0 V to 31 V with the prosthesis for the 8 element transducer. For the 16 element transducer, voltages ranged from 0 V to 13 V (no prosthesis) and 0 V to 39.5 V (with prosthesis). Again, pressure waveforms were measured using a Tektronix TBS2000 series oscilloscope at a sample rate of 500 MS/s, averaged over 128 pulses, and recorded in MATLAB.

To characterize the effects of the prosthesis at treatment-relevant pressures, high-pressure waveforms were also collected using a custom-built fiber optic probe hydrophone (FOPH) cross-calibrated against the rod hydrophone [Fig. 2(b), (d)]. A similar experimental approach was used. First, the FOPH was aligned to the transducer focus in free-field. Then, focal pressure waveforms were measured for each transducer with and without the prosthesis using a Tektronix TBS2000 series oscilloscope at a sample rate of 500 MS/s and recorded in MATLAB. A range of driving voltages were tested until an estimated p- of $\sim$20 MPa or the maximum transducer voltage (250 V) was reached. Tested

driving voltages in free-field ranged from 0 V to 100 V for the 8 element transducer and 0 V to 70 V for the 16 element transducer. Across the prosthesis, driving voltages of 0 V to 250 V were tested for both transducers. Due to the decreased signal-to-noise ratio expected for waveforms recorded using the FOPH, waveform averaging was increased to 512 pulses for all FOPH measurements.

For all prosthesis tests, the prosthesis was mounted within a 3D-printed "mock skull" to mimic any potential shielding effects caused by the skull at the periphery of the prosthesis in an *in vivo* setting [Fig. 2]. *P-* were calculated from each waveform, averaged, and compared between conditions. As with single element tests, individual data points were excluded from analysis if the *p-* was not clearly distinguishable from noise in the recorded waveform. Within each condition, *p-* measurements were averaged using separate rod hydrophone and FOPH data sets, as well as combined rod and fiber data, to distinguish any pressure loss differences at high and low pressures.

2) Aberration Correction: To correct for possible aberration distortions to the histotripsy therapy pulse caused by the prosthesis, a hydrophone-based aberration correction (AC) technique was applied to realign the arrival times of the *p-* from individual transducer elements for each of the array transducers. First, the FOPH was aligned to the transducer focus in degassed water under free-field. Then, the cranial prosthesis was placed perpendicularly between the transducer and the hydrophone. Next, each element of the transducer was fired individually at subthreshold *p-*, with the resulting waveform recorded in MATLAB and averaged over 512 pulses. A custom MATLAB script was then used to realign the arrival times of the pressure waveforms by correcting the phase delay of each element. These corrections were sent to the FPGA signal generator driving the histotripsy transducer, and FOPH tests were repeated with aberration correction applied for both the 8 element and 16 element transducers as described above. Driving voltages of 0 V to 250 V and 0 V to 215 V were tested for the 8 element and 16 element transducers, respectively.

3) Optical Imaging of Cavitation Bubble Clouds: Optical imaging was used to characterize the bubble clouds generated by the 8 element and 16 element transducers in degassed water with and without the prosthesis in the pressure field as well as with and without aberration correction. To accomplish this, a Photron high-speed camera (Nova S12 monochrome, Proprietary Design Advanced CMOS, Photron USA, Inc., San Diego, CA, USA) attached to an 85 mm f/2.81-5x super-macro lens (Creator, Mitakon Zhongyi, Liaoning Province, CHN) was aligned across from a continuous LED light source (Multi-LED QT Light, MultiLED G8 controller, 320 W power supply, GS Vitec Soden-Salmünster, Germany) [Fig. 2(e)]. After centering the histotripsy bubble cloud within the camera's field of view, 100 pulses were delivered at pulse repetition frequencies (PRFs) of 1 Hz, 5 Hz, 10 Hz, 50 Hz, 100 Hz, 500 Hz, and 1000 Hz, and resulting bubble clouds were imaged. For each pulse, the Photron camera was triggered by the histotripsy system's FPGA controller board at either 36.5 µs (8 element) or 46.5 µs (16 element) after pulse firing to collect an image of the bubble cloud mid-expansion (5.8 µs and 7.3 µs after the expected pulse arrival at the focus for the 8 element and 16 element transducers, respectively). Finally, images were qualitatively analyzed and compared between conditions (no prosthesis, prosthesis no AC, prosthesis with AC). For water tests, the camera frame rate was set to 12800 frames per second with an image resolution of 1024 × 1024.

4) Agarose Gel Phantom Experiments: To determine whether histotripsy bubble clouds could be generated across the prosthesis, 1% weight/volume (w/v) agarose gel phantoms were prepared to mimic the viscoelastic properties of soft tissue as previously described [36], [40]. To create the agarose gel phantom, 0.5% agarose powder (Type VII-A, Sigma Aldrich Corporation, St. Louis, MO, USA) was stirred into 99.5% deionized water at room temperature until thoroughly mixed. Then, the mixture was heated to boiling using a microwave oven and stirred to induce flash boiling, releasing dissolved gas from the mixture. This boiling and stirring process was repeated until approximately 50% of the solution volume remained, giving a degassed 1% w/v agarose gel mixture. Next, the gel mixture was placed in a vacuum desiccator and maintained under pressure until the temperature of the agarose solution cooled to <40 °C. After cooling, 100 mL of the solution was pipetted into a rectangular silicon mold fitted with a custom-designed poly-lactic acid (PLA) phantom mount and placed in a refrigerator for one hour to solidify.

After securing the agarose phantom to the computer-guided 3D robotic positioner, the gel was steered into the focus of the transducer (either 8 element or 16 element) so that the bubble cloud was fully contained within the gel [Fig. 2(e)]. Then, 100 pulses were delivered to the gel at PRFs of 1 Hz, 5 Hz, 10 Hz, 50 Hz, 100 Hz, 500 Hz, and 1000 Hz at a driving voltage of 250 V (estimated free-field *p-* of ∼29 MPa (8 element) or ∼47 MPa (16 element)), and resulting bubble clouds were imaged using the high-speed camera set-up described above. Images were again qualitatively analyzed and compared between conditions (no prosthesis, prosthesis no AC, prosthesis with AC). For all agarose tests, the camera frame rate was set to 12800 frames per second with an image resolution of 1024 x 1024.

5) Red Blood Cell Phantom Ablation: To test the ablative potential of the histotripsy bubble clouds generated across the prosthesis, red blood cell (RBC) phantoms were fabricated as previously described and used for ablation experiments [36], [41], [42], [43], [44]. To create the RBC phantoms, a 1% w/v agarose mixture was produced using the methods described above, substituting 0.9% saline in place of deionized water. An initial layer of agarose was poured into the silicone mold and refrigerated to create the base layer of the RBC phantom. For the second layer, fresh porcine blood was obtained from a local abattoir and added to an anticoagulant solution of Citrate Phosphate Dextrose Anticoagulant (CPD, Sigma Aldrich Corporation, St. Louis, MO, USA) at a ratio of 1 mL CPD: 9 mL blood. To separate the RBCs from unneeded blood components, whole blood was centrifuged at 3000 RCF for 15 minutes; then, 0.5 mL of RBCs were isolated and combined with 9.5 mL of the agarose solution. Next, the liquid RBC-agarose solution was poured onto the base layer and tilted to thoroughly coat the entire gel surface. Excess solution was immediately discarded

via inversion, leaving behind a thin layer of the RBC-agarose solution. After placing the middle layer and refrigerating for 3 minutes, the remaining agarose without RBCs was poured on top of the bottom two layers to fill the silicone mold and allowed to solidify in the refrigerator for one hour before use.

For ablation efficacy experiments, only the 16 element histotripsy transducer was used due to its ability to generate comparatively higher p- across the prosthesis. First, the RBC phantom was mounted onto the 3D robotic positioner and steered into the focus of the transducer, and the RBC layer was aligned with the center of the bubble cloud. Then, histotripsy pulses were delivered to the gel at therapy-relevant PRFs of 100 Hz and 500 Hz at the transducer's maximum driving voltage (250 V) across the prosthesis with and without aberration correction (corresponding to estimated p- of ∼22 MPa and ∼13.5 MPa, respectively). To generate effective ablation of the RBCs, 2000 histotripsy pulses were applied for all tests with and without the prosthesis. N = 4 RBC phantoms were tested for each condition.

RBC experiments were imaged using the high-speed camera set-up described above with a frame rate of 22500 frames per second and an image resolution of 512 x 1024. Two images were collected for each histotripsy pulse to characterize both the bubble cloud and resulting RBC ablation.

6) Excised Porcine Brain Ablation: To mimic an *in vivo* histotripsy ablation, additional experiments were completed targeting excised porcine brain tissues with histotripsy across the prosthesis. First, a whole pig brain was obtained from a local abattoir and degassed inside of a saline solution in a vacuum chamber for >2 hours. Then, the brain was sectioned into four pieces, and each section was embedded in a 7.5% gelatin in degassed saline (Gelatin from porcine skin, Sigma Aldrich, St. Louis, MO, USA) tissue phantom for treatment. After solidifying the gel via refrigeration, phantoms containing brain sections were mounted onto the 3D robotic positioner and steered into the focus of the transducer. Next, histotripsy ablations were applied across the prosthesis to 5 mm x 5 mm x 5 mm cubes fully contained within each tissue using the 16 element transducer, a PRF of 500 Hz, and an estimated peak negative pressure of ∼22 MPa (across the prosthesis; corresponds to 250 V, the transducer's maximum driving voltage). To maximize the ablative potential of the treatment, all tissues were treated with aberration correction at 2000 pulses per treatment location. Treatment points were spaced by 1.25 mm in the axial direction and 0.5 mm in the lateral and elevational directions to allow overlap between the bubble clouds at each location. All samples were treated within 36 hours of harvest and within 24 hours of phantom preparation.

After treatment, treated tissues were visually inspected and fixed in 10% formalin for a minimum of 24 hours post-treatment before sectioning and staining. To assess the microscopic damage caused by the histotripsy treatment across the prosthesis, a standard hematoxylin and eosin (H&E) stain was used for all tissues.

7) Ultrasound Imaging of Cavitation Bubble Clouds: To determine whether the histotripsy bubble cloud could be visualized across the prosthesis using ultrasound, real-time ultrasound images were also collected using the coaxially aligned ultrasound imaging probe fixed within the 16 element transducer during all experiments.

TABLE II
SINGLE ELEMENT PRESSURE LOSS (MEAN ± STANDARD DEVIATION) THROUGH THE PROSTHESIS SORTED BY FREQUENCY AND ANGLE

Frequency	Average Pressure Loss Through Prosthesis		
	90°	*120°*	*135°*
500 kHz	9.09 ± 0.49%	18.63 ± 1.02%	38.10 ± 0.93%
1 MHz	15.43 ± 1.31%	25.51 ± 1.65%	56.70 ± 1.34%
3 MHz	23.46 ± 3.50%	39.88 ± 3.31%	85.91 ± 1.35%

III. RESULTS

A. Single Element Findings

1) Beam Profile and Pressure Waveform Characterization: Under perpendicular conditions (90°), average pressure losses of 9.09 ± 0.49%, 15.43 ± 1.31%, and 23.46 ± 3.50% were calculated across the prosthesis for 500 kHz, 1 MHz, and 3 MHz transducers, respectively. Interestingly, large differences in pressure loss were identified at increasing prosthesis angles relative to the transducer for all frequencies. The findings for each of the single element transducers are summarized in Table II and plotted in Fig. 3(d). At 500 kHz, average pressure losses of 18.63 ± 1.02% and 38.10 ± 0.93% were measured at angles of 120° and 135° relative to the prosthesis, respectively. For the 1 MHz transducer, an average pressure loss of 25.51 ± 1.65% was observed at 120°; at 135°, 56.70 ± 1.34%. Tests using the 3 MHz transducer yielded an average pressure loss of 39.88 ± 3.31% at 120° and 85.91 ± 1.35% at 135°. Additionally, a pre-focal shift in the waveform arrival time was observed for all pressure waveforms collected across the prosthesis relative to free-field, with no clear differences observed between test angles [Fig. 3(a)–(c)]. The speed of sound through the prosthesis was calculated using the pre-focal shift in the waveform arrival time for all three frequencies, giving estimated sound speeds of 2472 m/s, 2234 m/s, and 2082 m/s for the 500 kHz, 1 MHz, and 3 MHz transducers, respectively.

As expected, all beam profiles reflected notable peak positive and peak negative pressure reductions at the focus across the prosthesis [**Supplementary Fig. 1**]. While transverse beam profiles remained relatively unchanged in space at all frequencies and angles, elevational beam profiles were affected by prosthesis angle across all frequencies, shifting post-focally relative to the geometric focus of the transducer with increasing angle. Elevational beam profiles experienced greater post-focal shifting for higher frequencies. Taken together, these findings demonstrate that ultrasonic transmission across the prosthesis is angle-dependent as well as frequency-dependent and suggest clinically-relevant histotripsy array transducers with multiple elements may experience increased pressure loss and beam distortions across the prosthesis.

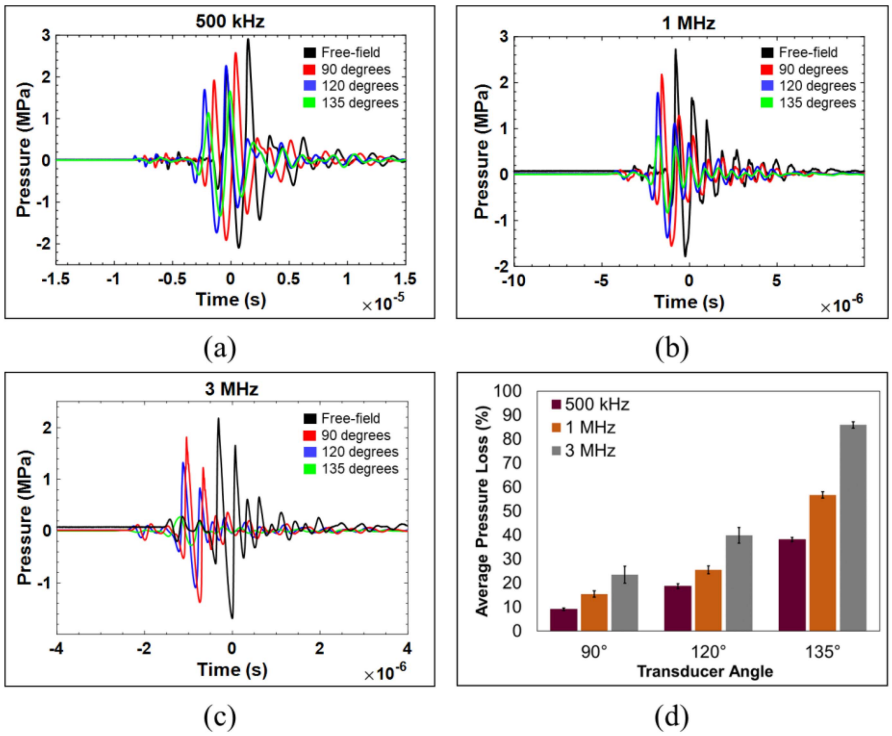

Fig. 3. Single element findings. (a)–(c) Representative pressure waveforms collected in free field and test conditions for 500 kHz, 1 MHz, and 3 MHz single element transducers, respectively. (d) Average single element pressure loss through the prosthesis plotted by frequency and angle.

TABLE III
AVERAGE PRESSURE LOSSES AND MAXIMUM ACHIEVABLE PEAK NEGATIVE PRESSURES FOR THE 8 ELEMENT AND 16 ELEMENT HISTOTRIPSY ARRAY TRANSDUCERS THROUGH THE PROSTHESIS

Transducer	Average Pressure Loss		Maximum Achievable *P*-		
	Without AC	*With AC*	*No Prosthesis*	*With Prosthesis Without AC*	*With Prosthesis With AC*
8 element	59.12 ± 1.87%	46.69 ± 2.14%	28.85 MPa	13.42 MPa	18.96 MPa
16 element	77.97 ± 1.68%	59.68 ± 4.74%	47.29 MPa	13.42 MPa	22.15 MPa

Average pressure losses are reported for the entire range of voltages tested for each transducer (mean ± standard deviation). Maximum achievable *p*- were calculated using either extrapolation (> 20 MPa) or pressure waveforms recorded with the FOPH at 250 V (< 20 MPa). AC = aberration correction.

B. Multi-Element Array Transducer Findings

1) Beam Profile and Pressure Waveform Characterization: For the 8 element transducer, average pressure losses across the prosthesis were measured to be 59.81 ± 0.92% and 58.62 ± 1.59% using the rod hydrophone and FOPH, respectively, while the 16 element transducer experienced average pressure losses of 77.81 ± 1.83% (rod) and 78.09 ± 1.57% (FOPH). No differences were measured between average low- and high-pressure loss values for either transducer, yielding an average pressure loss of 59.12 ± 1.87% and 77.97 ± 1.68% across the entire range of voltages tested for the 8 and 16 element transducers, respectively.

Aberration correction for the 8 element transducer resulted in an average pressure recovery of 11.94 ± 1.11%, reducing the average pressure loss across the prosthesis to 46.69 ± 2.14%. For the 16 element transducer, an average pressure recovery of 18.29 ± 4.21% was achieved with aberration correction, resulting in an average loss of 59.68 ± 4.74% across the prosthesis. Consistent with the single element tests, a pre-focal shift in the waveform arrival time was observed for pressure waveforms collected across the prosthesis relative to free-field for both array transducers, with and without AC [Fig. 4(a), (d)]. Maximum peak negative pressures achievable across the prosthesis with and without AC for the 8 and 16 element transducers are given in Table III.

Beam profile collection using the 8 element transducer revealed aberrations to the pressure field across the prosthesis in all three planes. While the axial beam profile was shifted pre-focally [**Supplementary Fig. 2**], the transverse and elevational profiles were shifted in the post-focal direction [Fig. 4(b)–(c)]. Transverse and elevational profiles also demonstrated a widening in the beam profile across the prosthesis, corresponding to an increase in the full-width half-maximum (FWHM) measurements

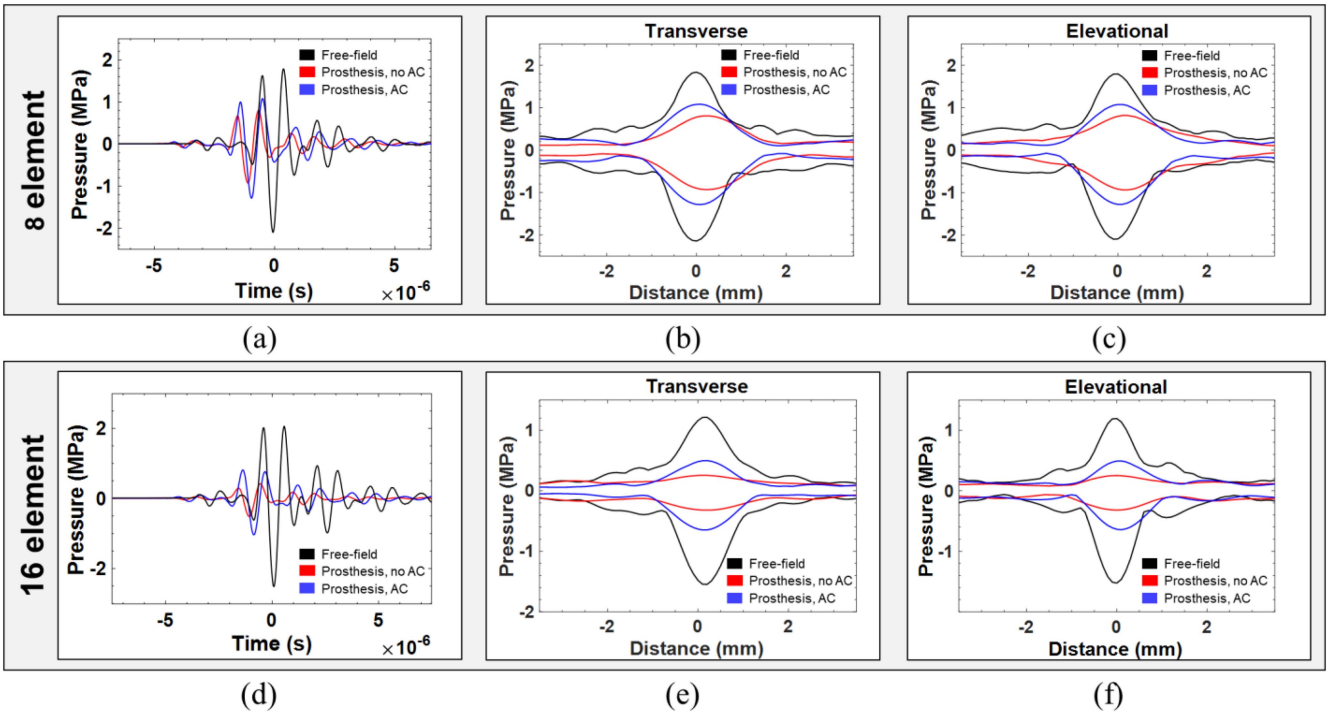

Fig. 4. Multi-element array transducer beam profile and pressure waveform collection. (a), (d) Representative pressure waveforms collected under free field and test conditions for the 8 and 16 element transducers, respectively. (b)–(c), (e)–(f) Beam profiles collected across test conditions for the 8 and 16 element transducers in the (b), (e) transverse, and (c), (f) elevational directions.

TABLE IV
FULL-WIDTH HALF-MAXIMUM (FWHM) VALUES CALCULATED USING PEAK NEGATIVE PRESSURE BEAM PROFILES COLLECTED FOR THE 8 AND 16 ELEMENT TRANSDUCERS WITH AND WITHOUT THE PROSTHESIS

Transducer	Transverse			Elevational		
	No Prosthesis	*With Prosthesis Without AC*	*With Prosthesis With AC*	*No Prosthesis*	*With Prosthesis Without AC*	*With Prosthesis With AC*
8 element	1.24 mm	1.95 mm	1.67 mm	1.26 mm	1.94 mm	1.68 mm
16 element	1.21 mm	2.18 mm	1.53 mm	0.96 mm	1.71 mm	1.32 mm

calculated using the peak negative pressure profiles for each condition.

Aberrations to the pressure field were also observed in all three planes for the 16 element transducer. Like the 8 element transducer, the axial beam profile of the 16 element transducer was shifted pre-focally across the prosthesis [**Supplementary Fig. 2**], and the transverse and elevational profiles were shifted post-focally [Fig. 4(e)–(f)]. Additionally, beam profiles in the transverse and elevational directions experienced widening across the prosthesis and had increased FWHM measurements [Table IV]. The application of aberration correction was able to overcome some of these effects for both transducers, narrowing the beam profiles, reducing FWHM [Table IV], and returning the profile minimum to a point closer to the transducer's geometric focus [Fig. 4(b) and (c), (e) and (f)**; Supplementary Fig. 2**].

2) Bubble Cloud Generation: Using the 8 element transducer fired across the prosthesis without AC, bubble clouds were generated in water at PRFs $\geq$ 100 Hz after several histotripsy pulses; by 100 pulses, robust bubble clouds had formed at 500 Hz and 1000 Hz. Comparatively, when fired across the prosthesis without AC in agarose, bubble clouds were observed at PRFs $\geq$ 50 Hz. For both water and gel conditions, bubble clouds were shifted pre-focally, were notably reduced in size, and grew more robust after several histotripsy pulses. After applying AC, bubble clouds were generated in water only at PRFs $\geq$ 500 Hz, but formed more quickly on average (by 10 pulses) and were noticeably denser. In gels with AC, bubble clouds were also observed at PRFs $\geq$ 500 Hz.

16 element findings closely resembled those of the 8 element transducer [Fig. 5(a) and (b)]. Without AC, bubble clouds were generated in water after 10 or more pulses at PRFs $\geq$ 50 Hz. At 50 Hz and 100 Hz, bubble clouds were sparse and ill-defined; at 500 Hz and 1000 Hz, bubble clouds were characterized by a long, dense core surrounded by sparse peripheral cavitation [Fig. 5(a), left]. In gels without AC, bubble clouds were consistently observed at PRFs $\geq$ 100 Hz [Fig. 5(a), right]. As observed using the 8 element transducer, bubble clouds without AC were shifted pre-focally, so a second set of cloud images were collected in

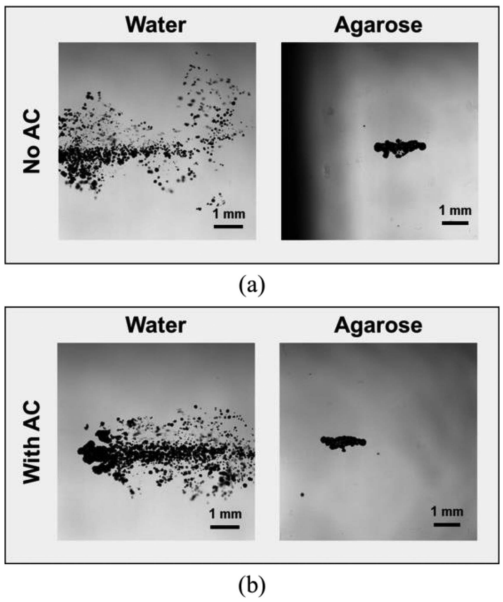

Fig. 5. Bubble cloud formation across the prosthesis. (a) and (b) Optical images of the bubble cloud generated through the prosthesis using the 16 element transducer with and without aberration correction (AC) at 250 V and 500 Hz. Due to a pre-focal shift in the bubble cloud location, the camera was manually repositioned to image bubble clouds through the prosthesis without AC. Blockage of the light source caused by the mock skull can be seen in the right image of (a).

gel by manually shifting the field of view of the camera. In repositioned gel images collected using the 16 element transducer, clearly visible, well-defined bubble clouds were generated by the tenth pulse for PRFs $\geq$ 100 Hz [Fig. 5(a), right]. Bubble clouds were notably reduced in size compared to free-field clouds, corresponding to the measured pressure reduction across the prosthesis. After applying AC, bubble clouds were generated in water at PRFs $\geq$ 500 Hz, but were noticeably denser and appeared to have less peripheral cavitation [Fig. 5(b), left]. In gels with AC, bubble clouds were sometimes observed at PRFs of 50 Hz and 100 Hz, but were consistently recorded at PRFs $\geq$ 500 Hz [Fig. 5(b), right]. Bubble clouds were comparable in size to non-AC clouds in gel and formed by the tenth pulse, growing into a fully formed cloud by 100 pulses. Bubble clouds in gel after AC were shifted closer to the geometric focus of the transducer, and manual repositioning of the camera was not required for image collection.

3) Ablation Feasibility: RBC Phantoms: Without applying AC, ablative damage to the RBCs was observed by 2000 pulses at 100 Hz and 500 Hz using the 16 element transducer [Fig. 6, row 1]. At both PRFs, lesions were elongated and linear in shape. The core of the lesion was ablated first and most completely, with peripheral damage increasing with the number of pulses applied. As expected from agarose gel tests, RBC lesions without AC were shifted pre-focally, and the camera was repositioned for the image acquisition.

After applying AC, ablative damage to the RBCs was notable by 2000 pulses at 100 Hz and 500 Hz [Fig. 6, row 2]. Markedly different bubble cloud behavior was observed between the two PRFs, however. For 100 Hz, early sparse cavitation condensed into a well-defined bubble cloud by 2000 pulses [Fig. 6, row 2, left]. At 500 Hz, sparse cavitation was observed from 0 to 2000 pulses. At 2000 pulses, a dense bubble core formed as the RBC layer was ablated, but peripheral cavitation persisted [Fig. 6, row 2, right].

4) Ablation Feasibility: Excised Brain: Histotripsy bubble clouds were generated in all excised brain tissues and clearly visualized on ultrasound imaging as oscillating hyperechoic regions [Fig. 7(b)]. Additionally, mild-to-moderate pre-focal cavitation was observed at the gel-tissue interface on ultrasound imaging for two of four samples at superficial treatment points. After histotripsy treatment, ablated portions of the tissue were characterized by a complete destruction of targeted cells and surrounding extracellular matrix and replacement by acellular debris [Fig. 7(c)–(e)]. Clear boundaries were observed between treated and untreated tissue regions [Fig. 7(c)].

IV. Discussion

This study investigated the feasibility of applying US-guided intracranial histotripsy procedures through a newly developed, biocompatible, polyolefin-based cranioplasty device. While previous studies have demonstrated the use of the prosthesis preclinically for ultrasound imaging [9], ultrasonic blood brain barrier (BBB) opening [10], and clinically for patient follow-up and long-term ultrasound surveillance for tumor recurrence [11], this is the first study to investigate the application of histotripsy across the prosthesis for tumor ablation. Through a series of single and multi-element histotripsy transducer tests, the feasibility of applying histotripsy across the prosthesis was demonstrated despite significant pressure attenuation. Histotripsy bubble clouds were generated across the prosthesis in water and tissue-mimicking agarose gels at high pulse repetition frequencies (PRFs), and red blood cells were successfully ablated over thousands of pulses in an agarose-based phantom. Then, excised porcine brain tissues were targeted across the prosthesis to demonstrate clinical feasibility, with complete cellular and matrix breakdown observed histologically following histotripsy. During all treatments, bubble clouds could be visualized in real-time across the prosthesis using ultrasound, further suggesting that the cranioplasty device may be used as an acoustic window through which intracranial ultrasound-guided histotripsy therapies can be applied.

Single element findings from this study closely matched results from previous work characterizing ultrasonic energy transmission across the prosthesis when the transducer was aligned perpendicularly to the prosthesis [9]. Both studies identified considerably higher energy transmission across the prosthesis (~76%–90%) compared to intact cranial bone (<1%–31% depending on skull thickness [45], [46]), with transducers of increasing frequency experiencing higher pressure loss. The current study expanded upon these initial observations by testing single element transducers at different angles relative to the prosthesis, mimicking the various element angles in a multi-element histotripsy array transducer. Interestingly, a significant increase in pressure loss was measured across the prosthesis at increasing angles for the first time using the single element

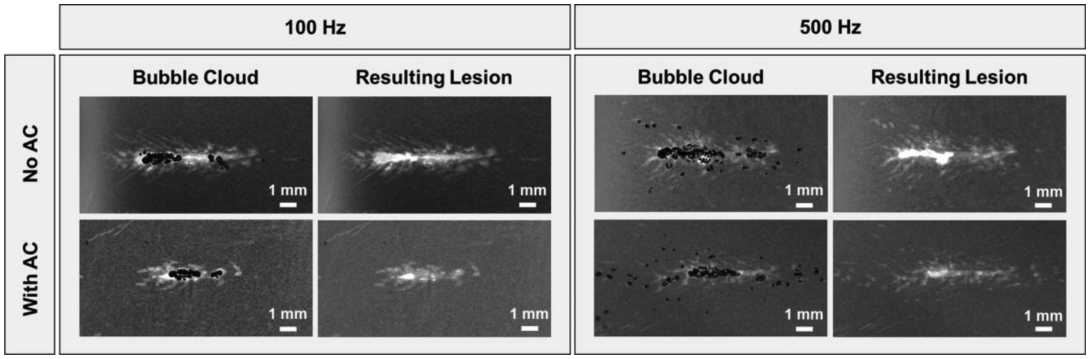

Fig. 6. Optical images of the red blood cell ablation achieved through the prosthesis at 250 V and 2000 pulses using the 16 element transducer. Through the prosthesis without aberration correction (AC), ablative damage to the RBCs was observed by 2000 pulses at 100 Hz and 500 Hz, but was sparse and varied between gels. With AC, more predictable cavitation was observed at 100 Hz, but significant peripheral cavitation was still seen at 500 Hz PRF.

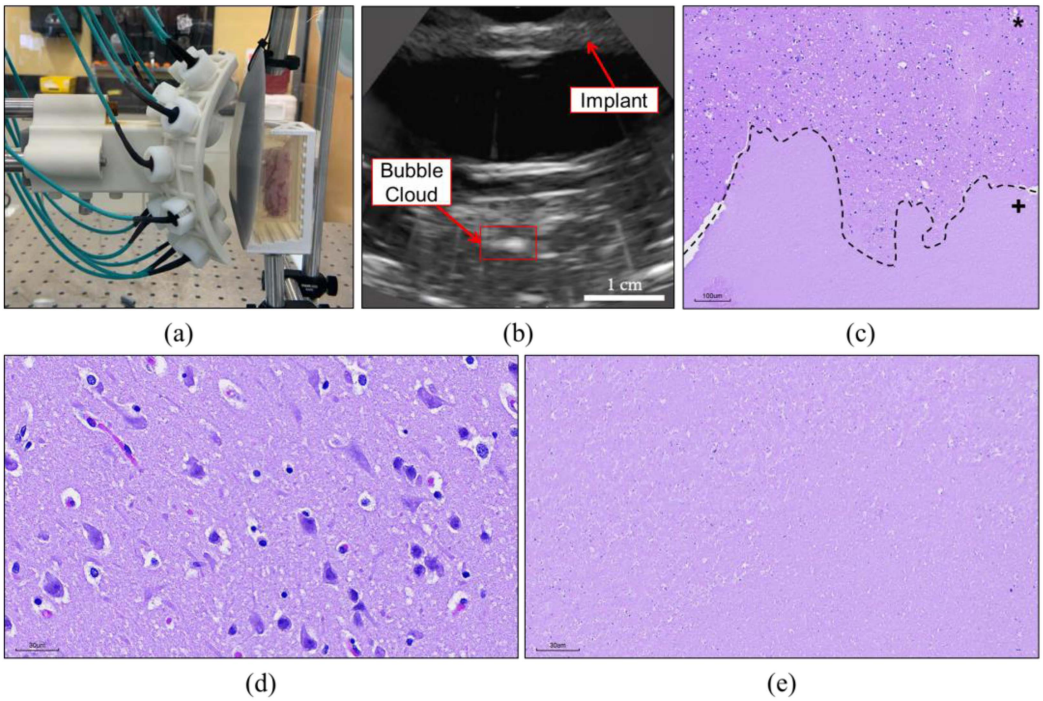

Fig. 7. Excised brain ablation through the prosthesis using the 16 element transducer at 250 V, 500 Hz, and 2000 pulses per treatment location. (a) Excised brain tissue encased in gelatin and aligned to the focus of the transducer with the prosthesis in the pressure field. (b) Real-time ultrasound image collected through the prosthesis during an excised tissue ablation. Minimal distortion was observed through the prosthesis, and the histotripsy bubble cloud was clearly visualized. (c)–(e) Hematoxylin & eosin staining of the treatment boundary (c – magnification: 20x) and corresponding untreated (d) – magnification: 40x) and treated ((e)– magnification: 40x) tissue regions for one brain sample. A complete loss of cellular and extracellular matrix structures is observed in the treated tissues (e).

transducers, suggesting that clinically-relevant multi-element histotripsy array transducers, which typically have a subset of their elements aligned at steep angles, may experience greater pressure loss across the prosthesis than previously expected [9].

To further investigate this hypothesis, US transmission across the prosthesis was tested using an 8 element, 1 MHz histotripsy transducer. For this transducer, an average pressure loss of $>50\%$ was measured, greater than the reduction measured for a single, perpendicularly-aligned 1 MHz element, but falling within the range predicted by the 1 MHz single element angle measurements. Beam profiles collected with the 8 element transducer showed a widening of transverse and elevational profiles and an increase in their full-width half-maximum (FWHM), likely due to an prosthesis-generated dephasing in the arrival time of pressure waveforms from elements positioned at different angles. Additionally, there was a repeatable pre-focal shift in the axial profile. Using a hydrophone-based aberration correction (AC) technique, some of the pressure lost for the 8 element transducer was restored, with a corresponding decrease in the transverse and elevational profile FWHMs and a reduction of the pre-focal axial shift in the focal location. Even with AC, the maximum estimated peak negative pressure (p-) achievable across the prosthesis with

the 8 element transducer was ∼19 MPa, lower than the previously measured intrinsic histotripsy threshold in water-based soft tissues and blood, which ranges from 26–30 MPa [14], [47]. To reach a higher p- across the prosthesis, tests were repeated with a 16 element transducer. For the 16 element transducer, an average pressure loss >75% was measured before aberration correction, likely due to the increased number of elements positioned at steep angles relative to the prosthesis within the transducer. After applying AC, some pressure recovery was observed, resulting in a maximum estimated p- of ∼22 MPa across the prosthesis for the 16 element transducer. AC also reduced transverse and elevational FWHM values for this transducer, reflecting a refocusing of the respective beam profiles, and reduced the axial pre-focal shift. Notably, increased ultrasonic pressure transmission was measured across the prosthesis for both transducers (up to 54% with AC) than previously reported for the skull (<1%–3%) [46], [48].

Despite high pressure attenuation and sub-intrinsic threshold p- achievable with the current devices, results from cavitation and ablation experiments revealed that histotripsy bubble clouds were capable of achieving effective ablation across the prosthesis at clinically-relevant PRFs (≥ 50 Hz). Bubble clouds across the prosthesis, however, were notably reduced in size compared to free-field for all conditions (as expected given the comparatively lower p-) and took multiple histotripsy pulses to fully develop, mimicking recent findings which describe the behavior of histotripsy bubble clouds generated using single cycle pulses at PRFs ≥ 100 Hz [49]. In the referenced study, dense bubble clouds were generated by the tenth pulse at p- as low as 20 MPa for PRFs of 100 Hz and 1000 Hz [49].

Further studies are warranted investigating histotripsy across the prosthesis. First, histotripsy device improvements are needed, increasing the maximum p- possible across the prosthesis to generate more efficient, predictable ablation. Alternatively, techniques to reduce the cavitation threshold of the target tissue could be investigated, such as injecting nanoparticles into the tumor prior to treatment. Past studies have demonstrated that nanoparticle-mediated histotripsy (NMH) can generate bubble clouds at pressures significantly below the intrinsic threshold of water (≥10 MPa) and can create precise ablation zones [40], [50]. Using NMH in conjunction with the prosthesis may allow more predictable, robust bubble clouds to be formed across the prosthesis during histotripsy therapies. This NMH approach could also be combined with tumor-trapping hydrogels that have recently been developed by our team for use after brain tumor surgery, allowing for an attract-and-treat histotripsy approach for the ablation of recurrent brain tumors [51]. Finally, improved histotripsy devices or NMH should be used to investigate the *in vivo* safety and feasibility of applying histotripsy for brain tumor ablation across the prosthesis.

Other factors to consider prior to clinical translation of this approach include potential heating of the prosthesis, the contribution of shear mode conversion to the measured pressure loss, and the observed axial pre-focal shift in bubble cloud formation. While unlikely at the low duty cycles used for histotripsy, heating of the prosthesis during therapy is possible, particularly for techniques which utilize longer pulse durations such as thermal high intensity focused ultrasound, and could lead to off-target injury. The conversion of the applied ultrasound to shear waves at the prosthesis interface may contribute to this effect and should be quantified in future work. Likewise, shear mode conversion may also be partially responsible for the pressures losses and other focal changes observed across the prosthesis in this study, especially at steep angles. The pre-focal shift in the bubble cloud along the transducer's axis observed in this study could lead to mistargeting if not corrected for and should be accounted for in the pre-treatment planning process.

V. Conclusion

This study investigated the *in vitro* feasibility of applying US-guided intracranial histotripsy procedures through a newly developed, biocompatible, polyolefin-based cranioplasty device using single and multi-element histotripsy transducers. Single element results revealed an angle- and frequency-dependent effect of the prosthesis on ultrasound transmission, and multi-element histotripsy array findings demonstrated reduced pressure transmission across the prosthesis, albeit higher than through the skull, and a widening of beam profiles. High speed imaging in gel phantoms and ultrasound imaging in excised brain tissues showed that histotripsy bubble clouds capable of ablation could be generated across the prosthesis at high pulse repetition frequencies, and a complete breakdown of targeted cells and matrix was observed histologically in all treated tissues. Overall, the results of this study lay the groundwork for future advancements in ultrasound-guided histotripsy for intracranial applications, particularly in settings where MRI access is limited.

Acknowledgment

The authors would like to thank Alex Simon for his assistance with agarose gel and RBC experiments and other members of the Vlaisavljevich Research Laboratory for their assistance and support.

Eli Vlaisavljevich has an ongoing research partnership and financial relationship with HistoSonics, Inc. Lauren Ruger has an ongoing consulting relationship with Theraclion. Francesco Prada is a patentholder of the cranial prosthesis used throughout the study and is a stockholder of Intelligenza Trasparente S.R.L., the company which manufactures the cranioplasty device. No other authors have a conflict of interest to report.

References

[1] V. Krishna, F. Sammartino, and A. Rezai, "A review of the current therapies, challenges, and future directions of transcranial focused ultrasound technology: Advances in diagnosis and treatment," *JAMA Neurol.*, vol. 75, no. 2, pp. 246–254, 2018, doi: 10.1001/jamaneurol.2017.3129.

[2] J. Aubry and M. Tanter, "MR-guided transcranial focused ultrasound," *Adv. Exp. Med. Biol.*, vol. 880, pp. 97–111, 2016, doi: 10.1007/978-3-319-22536-4_6.

[3] F. Mueller et al., "Computational exploration of wave propagation and heating from transcranial focused ultrasound for neuromodulation," *J. Neural. Eng.*, vol. 13, no. 5, 2016, Art. no. 056002, doi: 10.1088/1741-2560/13/5/056002.

[4] G. Pinton et al., "Attenuation, scattering, and absorption of ultrasound in the skull bone," *Med. Phys.*, vol. 39, no. 1, pp. 299–307, 2012, doi: 10.1118/1.3668316.

[5] M. Gutierrez et al., "Novel cranial implants of yttria-stabilized zirconia as acoustic windows for ultrasonic brain therapy," *Adv. Healthcare Mater.*, vol. 6, no. 21, 2017, Art. no. 1700214, doi: 10.1002/adhm.201700214.

[6] F. Fry and J. Barger, "Acoustical properties of the human skull," *J. Acoust. Soc. Amer.*, vol. 63, no. 5, pp. 1576–1590, 1978, doi: 10.1121/1.381852.

[7] M. Belzberg et al., "Sonolucent cranial implants: Cadaveric study and clinical findings supporting diagnostic and therapeutic transcranioplasty ultrasound," *J. Craniofacial Surg.*, vol. 30, no. 5, pp. 1456–1461, 2019, doi: 10.1097/SCS.0000000000005454.

[8] J. Tobias et al., "An ultrasound window to perform scanned, focused ultrasound hyperthermia treatments of brain tumors," *Med. Phys.*, vol. 14, no. 2, pp. 228–234, 1987, doi: 10.1118/1.596074.

[9] F. Prada et al., "In vitro and in vivo characterization of a cranial window prosthesis for diagnostic and therapeutic cerebral ultrasound," *J. Neurosurg.*, vol. 134, pp. 646–658, 2020, doi: 10.3171/2019.10.JNS191674.

[10] L. Librizzi et al., "Ultrasounds induce blood-brain barrier opening across a sonolucent polyolefin plate in an in vitro isolated brain preparation," *Sci. Rep.*, vol. 12, no. 1, 2022, Art. no. 2906, doi: 10.1038/s41598-022-06791-7.

[11] M. Bene et al., "Cranial sonolucent prosthesis: A window of opportunity for neuro-oncology (and neuro-surgery)," *J. Neuro-Oncol.*, vol. 156, no. 3, pp. 529–540, 2022, doi: 10.1007/s11060-021-03929-x.

[12] K. Bader, E. Vlaisavljevich, and A. Maxwell, "For whom the bubble grows: Physical principles of bubble nucleation and dynamics in histotripsy ultrasound therapy," *Ultrasound Med. Biol.*, vol. 45, no. 5, pp. 1056–1080, 2019, doi: 10.1016/j.ultrasmedbio.2018.10.035.

[13] E. Vlaisavljevich et al., "Visualizing the histotripsy process: Bubble cloud-cancer cell interactions in a tissue-mimicking environment," *Ultrasound Med. Biol.*, vol. 42, no. 10, pp. 2466–2477, 2016, doi: 10.1016/j.ultrasmedbio.2016.05.018.

[14] Z. Xu et al., "Histotripsy: The first noninvasive, non-ionizing, non-thermal ablation technique based on ultrasound," *Int. J. Hyperthermia*, vol. 38, no. 1, pp. 561–575, 2021, doi: 10.1080/02656736.2021.1905189.

[15] Z. Xu et al., "Controlled ultrasound tissue erosion," *IEEE Trans. Ultrason., Ferroelect., Freq. Control*, vol. 51, no. 6, pp. 726–736, Jun. 2004, doi: 10.1109/tuffc.2004.1308731.

[16] J. E. Parsons et al., "Pulsed cavitational ultrasound therapy for controlled tissue homogenization," *Ultrasound Med. Biol.*, vol. 32, no. 1, pp. 115–129, 2006, doi: 10.1016/j.ultrasmedbio.2005.09.005.

[17] K.-W. Lin et al., "Histotripsy beyond the instrinsic cavitation threshold using very short ultrasound pulses: Microtripsy," *IEEE Trans. Ultrason., Ferroelect., Freq. Control*, vol. 61, no. 2, pp. 251–265, Feb. 2014, doi: 10.1109/TUFFC.2014.6722611.

[18] W. W. Roberts, "Development and translation of histotripsy: Current status and future directions," *Curr. Opin. Urol.*, vol. 24, no. 1, pp. 104–110, 2014, doi: 10.1097/MOU.0000000000000001.

[19] G. Schade et al., "Histotripsy focal ablation of implanted prostate tumor in an ACE-1 canine cancer model," *J. Urol.*, vol. 188, no. 5, pp. 1957–1964, 2012, doi: 10.1016/j.juro.2012.07.006.

[20] G. Schade et al., "Boiling histotripsy ablation of renal cell carcinoma in the eker rat promotes a systemic inflammatory response," *Ultrasound Med. Biol.*, vol. 45, no. 1, pp. 137–147, 2019, doi: 10.1016/j.ultrasmedbio.2018.09.006.

[21] A. Hendricks-Wenger et al., "Histotripsy ablation alters the tumor microenvironment and promotes immune system activation in a subcutaneous model of pancreatic cancer," *IEEE Trans. Ultrason., Ferroelect., Freq. Control*, vol. 68, no. 9, pp. 2987–3000, Sep. 2021, doi: 10.1109/TUFFC.2021.3078094.

[22] A. Hendricks-Wenger et al., "Histotripsy for the treatment of cholangiocarcinoma liver tumors: In vivo feasibility and ex vivo dosimetry study," *IEEE Trans. Ultrason., Ferroelect., Freq. Control*, vol. 68, no. 9, pp. 2953–2964, Sep. 2021, doi: 10.1109/TUFFC.2021.3073563.

[23] J. Vidal-Jove et al., "First-in-man histotripsy of hepatic tumors: The THERESA trial, a feasibility study," *Int. J. Hyperthermia*, vol. 39, no. 1, pp. 1115–1123, 2022, doi: 10.1080/02656736.2022.2112309.

[24] T. Worlikar et al., "Histotripsy for non-invasive ablation of hepatocellular carcinoma (HCC) tumor in a subcutaneous xenograft murine model," in *Proc. IEEE 40th Annu. Int. Conf. Eng. Med. Biol. Sociol.*, 2018, pp. 6064–6067, doi: 10.1109/EMBC.2018.8513650.

[25] N. Lu et al., "Transcranial MR-guided histotripsy system," *IEEE Trans. Ultrason., Ferroelect., Freq. Control*, vol. 68, no. 9, pp. 2917–2929, Sep. 2021, doi: 10.1109/TUFFC.2021.3068113.

[26] Y. Kim et al., "Transcranial histotripsy therapy: A feasibility study," *IEEE Trans. Ultrason., Ferroelect., Freq. Control*, vol. 61, no. 4, pp. 582–593, Apr. 2014, doi: 10.1109/TUFFC.2014.2947.

[27] J. Sukovich et al., "Real-time transcranial histotripsy treatment localization and mapping using acoustic cavitation emission feedback," *IEEE Trans. Ultrason., Ferroelect., Freq. Control*, vol. 67, no. 6, pp. 1178–1191, Jun. 2020, doi: 10.1109/TUFFC.2020.2967586.

[28] N. Lu et al., "Transcranial magnetic resonance-guided histotripsy for brain surgery: Pre-clinical investigation," *Ultrasound Med. Biol.*, vol. 48, no. 1, pp. 98–110, 2022, doi: 10.1016/j.ultrasmedbio.2021.09.008.

[29] J. Sukovich et al., "Targeted lesion generation through the skull without aberration correction using histotripsy," *IEEE Trans. Ultrason., Ferroelect., Freq. Control*, vol. 63, no. 5, pp. 671–682, May 2016, doi: 10.1109/TUFFC.2016.2531504.

[30] J. Sukovich et al., "In vivo histotripsy brain treatment," *J. Neurosurgery*, vol. 2018, pp. 1–8, 2020, doi: 10.3171/2018.4.JNS172652.

[31] T. Gerhardson et al., "Histotripsy mediated immunomodulation in a mouse GL261 intracranial glioma model," in *Proc. Int. Symp. Therapeutic Ultrasound*, 2018, doi: 10.13140/RG.2.2.19788.51845.

[32] N. Lu et al., "Two-step aberration correction: Application to transcranial histotripsy," *Phys. Med. Biol.*, vol. 67, no. 12, p. 125009, 2022, doi: 10.1088/1361-6560/ac72ed.

[33] J. R. Sukovich et al., "Neuronavigation-guided transcranial histotripsy, results in a cadaveric model," *J Acoust. Soc. Amer.*, vol. 152, 2022, Art. no. A154, doi: 10.1121/10.0015864.

[34] B. Hilabi, S. Alghamdi, and M. Almanaa, "Impact of magnetic resonance imaging on healthcare in low- and middle-income countries," *Cureus*, vol. 15, no. 4, 2023, Art. no. e37698, doi: 10.7759/cureus.37698.

[35] T. Gerhardson et al., "Histotripsy clot liquefaction in a porcine intracerebral hemorrhage model," *Neurosurgery*, vol. 86, no. 3, pp. 429–436, 2020, doi: 10.1093/neuros/nyz089.

[36] C. Edsall et al., "Effects of frequency on bubble-cloud behavior and ablation efficiency in intrinsic threshold histotripsy," *Phys. Med. Biol.*, vol. 66, no. 22, p. 225009, 2021, doi: 10.1088/1361-6560/ac33ed.

[37] J. E. Parsons, C. A. Cain, and J. B. Fowlkes, "Cost-effective assembly of a basic fiber-optic hydrophone for measurement of high-amplitude therapeutic ultrasound fields," *J. Acoustical Soc. Amer.*, vol. 119, no. 3, pp. 1432–1440, Mar. 2006, doi: 10.1121/1.2166708.

[38] J. Parsons et al., "Pulsed cavitational ultrasound therapy for controlled tissue homogenization," *Ultrasound Med. Biol.*, vol. 32, no. 1, pp. 115–129, 2005, doi: 10.1016/j.ultrasmedbio.2005.09.005.

[39] E. Vlaisavljevich et al., "Effects of f-number on the histotripsy intrinsic threshold and cavitation bubble cloud behavior," *Phys. Med. Biol.*, vol. 62, no. 4, pp. 1269–1290, 2017, doi: 10.1088/1361-6560/aa54c7.

[40] C. Edsall et al., "Bubble cloud behavior and ablation capacity for histotripsy generated from intrinsic or artificial cavitation nuclei," *Ultrasound Med. Biol.*, vol. 47, no. 3, pp. 620–639, 2021, doi: 10.1016/j.ultrasmedbio.2020.10.020.

[41] A. D. Maxwell et al., "A tissue phantom for visualization and measurement of ultrasound-induced cavitation damage," *Ultrasound Med. Biol.*, vol. 36, no. 12, pp. 2132–2143, 2010, doi: 10.1016/j.ultrasmedbio.2010.08.023.

[42] T. Y. Wang et al., "An efficient treatment strategy for histotripsy by removing cavitation memory," *Ultrasound Med. Biol.*, vol. 38, no. 5, pp. 753–766, 2012, doi: 10.1016/j.ultrasmedbio.2012.01.013.

[43] W. W. Roberts et al., "Histotripsy of the prostate using a commercial system in a canine model," *J. Urol.*, vol. 191, no. 3, pp. 860–865, 2014, doi: 10.1016/j.juro.2013.08.077.

[44] E. Vlaisavljevich et al., "Effects of f-number on the histotripsy intrinsic threshold and cavitation bubble cloud behavior," *Phys. Med. Biol.*, vol. 62, no. 4, pp. 1269–1290, 2017, doi: 10.1088/1361-6560/aa54c7.

[45] T. S. Riis, T. D. Webb, and J. Kubanek, "Acoustic properties across the human skull," *Ultrasonics*, vol. 119, 2022, Art. no. 106591, doi: 10.1016/j.ultras.2021.106591.

[46] S. Pfaffenberger et al., "Can a commercial diagnostic ultrasound device accelerate thrombolysis? An in vitro skull model," *Stroke*, vol. 36, no. 1, pp. 124–128, 2005, doi: 10.1161/01.STR.0000150503.10480.a7.

[47] A. D. Maxwell et al., "Probability of cavitation for single ultrasound pulses applied to tissues and tissue-mimicking materials," *Ultrasound Med. Biol.*, vol. 39, no. 3, pp. 449–465, 2013, doi: 10.1016/j.ultrasmedbio.2012.09.004.

[48] A. Y. Ammi et al., "Characterization of ultrasound propagation through ex-vivo human temporal bone," *Ultrasound Med. Biol.*, vol. 34, no. 10, pp. 1578–1589, 2008, doi: 10.1016/j.ultrasmedbio.2008.02.012.

[49] A. Simon et al., "Effects of pulse repetition frequency on bubble cloud characteristics and ablation in single-cycle histotripsy," *Phys. Med. Biol.*, vol. 69, no. 2, 2023, Art. no. 025018, doi: 10.1088/1361-6560/ad11a1.

[50] J. Khirallah et al., "Nanoparticle-mediated histotripsy (NMH) using perfluorohexane 'nanocones'," *Phys. Med. Biol.*, vol. 64, no. 12, 2019, Art. no. 125018, doi: 10.1088/1361-6560/ab207e.

[51] Z. M. Khan, "Development of an injectable hydrogel platform to capture and eradicate glioblastoma cells with chemical and physical stimuli," Doctoral dissertation, Dept. Biomed. Eng. Mechanics, Virginia Tech, Blacksburg, VA, USA, 2023.